ELSEVIER

Contents lists available at ScienceDirect

## Surface & Coatings Technology

journal homepage: www.elsevier.com/locate/surfcoat





# Microstructure and tribological property of laser cladding Stellite 6 alloy by laser remelting and ultrasonic surface rolling

Jiayu Sun<sup>a</sup>, Yingying Zhang<sup>a</sup>, Zhengyu Sun<sup>a</sup>, Tianbiao Yu<sup>a,\*</sup>, Guofa Wang<sup>a,b</sup>

- <sup>a</sup> School of Mechanical Engineering and Automation, Northeastern University, Shenyang 110819, China
- <sup>b</sup> School of Energy and Mining Engineering, China University of Mining and Technology, Beijing 100083, China

#### ARTICLE INFO

Keywords:
Laser cladding
Microstructure
Stellite 6
Laser remelting
USR
Friction and wear properties

## ABSTRACT

Stellite 6 alloy was deposited onto the surface of 27SiMn steel using the laser cladding (LC) technique, which was then followed by laser remelting (LR) and ultrasonic surface rolling (USR). The surface roughness, microstructure, microhardness, surface residual stress, and wear resistance of LC, LR, and LR-USR samples were studied using electron backscatter diffraction (EBSD), transmission electron microscopy (TEM), scanning electron microscopy (SEM), X-ray stress analyzer, Vickers hardness tester, and material surface performance tester. The results showed that compared with LC, LR-USR significantly refined the surface dendrites of the cladding layer, with the average dendrite size decreasing from 16.37  $\mu$ m to 6.92  $\mu$ m. After USR, the samples converted from tensile residual stress (TRS) to compressive residual stress (CRS), and the high-density dislocations and strain generated in the grains near the surface of the cladding layer. The wear depth volume of the LR-USR samples was the smallest, showing typical abrasive wear.

## 1. Introduction

Traditional subtractive manufacturing processes are complex and have low raw material utilization. Remanufacturing, as the ultimate form of recycling, restores high-value waste products to a pristine state, achieving significant energy savings and emission reduction benefits [1,2]. Moreover, the significant factors contributing to product component failure are wear and corrosion. Improper handling of failed parts in conventional manufacturing leads to considerable resource wastage and pollution [3]. However, with additive manufacturing increasingly applied across various industries, green manufacturing technologies emphasizing energy and material conservation are emerging [4].

Laser cladding technology represents an effective additive manufacturing method wherein materials with superior physical and chemical properties are utilized. This technique involves melting metal powder onto the surface of a workpiece through laser beam scanning, thereby enhancing the performance of repaired surfaces [5,6]. Even under the most challenging operating conditions, it provides effective protection for the substrate against both corrosion and abrasive wear [7–9], and facilitates the layer-by-layer construction of complex components. However, components produced by laser cladding often fail to

meet size and precision requirements and do not adequately address surface defects, such as cracks induced by thermal and residual stresses [10-12]. Therefore, exploring efficient post-processing techniques for laser cladding is of paramount practical significance.

Praharaj et al. [13] employed Laser Surface Remelting (LSR) as a post-processing to enhance the surface quality and tribological property of components prepared by Laser Directed Energy Deposition. The results indicated that LSR not only improved surface quality but also refined grain structure, thereby increasing hardness and wear resistance. Zhao et al. [14,15] milled laser cladding layers and investigated the chip morphology, mechanical property, and vibration. Zhang et al. [11,16] utilized laser cladding for the repair of hydraulic columns, followed by hard turning and rolling processes, analyzing the differences in plastic deformation mechanisms between laser cladding heterogeneous layered materials and bulk materials. The findings demonstrated that the rolling techniques achieved surface strengthening of the cladding layer, transforming tensile residual stresses into compressive residual stresses and improving corrosion resistance. Ye et al. [17] combined hard turning with ultrasonic surface rolling, introducing intense plastic deformation to enhance the surface performance of LC layers. The results indicated that USR treatment not only met precision requirements but also enhanced surface properties of laser cladding layers, achieving grain

E-mail address: tianbiaoyudyx@gmail.com (T. Yu).

<sup>\*</sup> Corresponding author.

refinement and work hardening effects. Wang et al. [18] subjected specimens of Ti6Al4V alloy prepared by selective laser melting (SLM) to three distinct post-processing techniques: heat treatment, ultrasonic surface rolling process (USRP), and direct current assisted ultrasonic surface rolling process (DC-USRP). The study revealed that DC-USRP samples demonstrated the lowest wear rate, and ultrasonic surface rolling increased hardness and transformed residual tensile stresses into residual compressive stresses. Hao et al. [19] studied the mechanism of the effect of USR on the mechanical properties of the Inconel 718 coating. After USRP, the microstructure of the coating surface was refined, and the intense plastic deformation increased the dislocation density and grain boundary density of the coating, increasing the surface hardness by 30 %; the wear rate decreased by 51 %, significantly improving the service life of H13 steel. Luo et al. [20] studied the effects of USR on the microstructure and properties of the surface layer of Ti6Al4V alloy. The results indicated that compared to the matrix, the grain size of the USR strengthened layer decreased, and the texture type changed. Grain refinement and dislocation strengthening led to an increase in microhardness and residual stress. Ou et al. [21] investigated the fretting friction and wear mechanisms of 20CrMoH steel under different experimental conditions using ultrasonic surface rolling. The results indicated that USR led to a significant increase in dislocations and martensitic transformation, enhancing microhardness and wear resistance, with the wear volume reduced by 92.05 % compared to the

In current research, the predominant post-processing techniques following laser cladding focus on achieving dimensional accuracy through turning technology. However, these methods are not only intricate but also contribute to significant resource wastage. In contrast, laser remelting (LR) technology not only alleviates thermal and residual stresses but also enhances surface roughness, thereby providing an excellent foundation for subsequent ultrasonic surface rolling (USR) techniques. Therefore, by subjecting the laser cladding layer to laser remelting followed by ultrasonic surface rolling, the entire process eliminates subtractive manufacturing. However, the surface quality of the coated preparation remains uncertain, and the anticipated outcomes of this approach are eagerly awaited.

This study focuses on hydraulic support column materials as substrates and proposes a novel surface remanufacturing process. Concerning the post-processing of laser cladding (LC), the methodology involves initial laser remelting (LR) followed by ultrasonic surface rolling (USR). Measurements encompass surface roughness, microstructure, microhardness, residual stress, and wear resistance across various sample surfaces. Furthermore, the experiments provide theoretical guidance for engineering applications in LC repair of hydraulic support columns and surface modification.

## 2. Experimental methods

#### 2.1. Materials and sample preparation

For the  $\varnothing20\times120$  mm cylindrical rod substrate of 27SiMn steel (0.24–0.32 wt% C, 1.1–1.4 wt% Si,  $\le$ 0.3 wt% Cr,  $\le$ 0.035 wt% S,  $\le$ 0.035 wt% P, 1.1–1.4 wt% Mn), the surface was prepared by polishing and cleaning, followed by LC remanufacturing. Fig. 1(a) illustrates the LC process and powder morphology. The LC processing parameters were as follows: laser power of 450 W, spot size of 2 mm, powder feed rate of 9 g/min, scanning speed of 6 mm/s, and overlap rate of 50 %. Stellite 6 powder (53 µm~100 µm, 0.9–1.4 wt% C, 0.7–1.55 wt% Si, 26–30 wt% Cr,  $\le$ 0.5 wt% Mn,  $\le$ 1 wt% Mo,  $\le$ 3 wt% Ni,  $\le$ 3 wt% Fe,  $\le$ 0.5 wt% Mn, balanced Co) was used. LR parameters were consistent with LC parameters. Fig. 2 depicts the schematic of the USR device, variable amplitude rod, and rolling tool tip. Utilizing the cold plasticity of metallic materials, the ultrasonic generator converts ordinary AC electricity into ultrasonic frequency oscillations, the transducer converts ultrasonic frequency oscillations into mechanical vibrations, and the variable

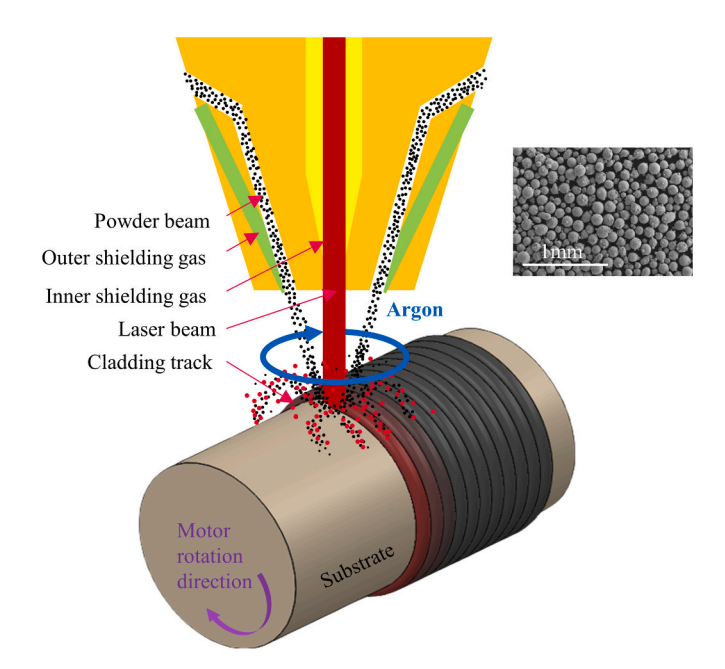


Fig. 1. LC process diagram and Stellite 6 powder morphology.

amplitude rod amplifies the transducer's amplitude, allowing the tool tip to impact the material surface at a frequency of 30KHz. Static force in the normal direction and ultrasound vibrations are applied to the surface of the material, resulting in significant compressive plastic deformation due to impact and extrusion effects. This result in peak shaving and valley filling on the sample surface, leading to an improved surface roughness [22]. The operating parameters were as follow: vibration frequency was 30 KHz, the load was 2000 N, feed speeds were 0.08 mm/rev, number of repeated processing is 8, and amplitude was 10  $\mu m$ . Three samples were prepared: laser cladding (LC) layer on cylindrical substrate, laser remelting (LR) after LC, and ultrasonic surface rolling (USR) after LR (LR-USR).

## 2.2. Microstructure characterization

The three samples were separately wire-electrode cut along the cross-section, polished with SiC sandpaper and diamond, cleaned in alcohol using ultrasonication, and dried, followed by a 60-s immersion in aqua regia. The microstructures of the LC, LR, and LR-USR sample cross-sections were characterized using field emission scanning electron microscopy (SEM; Zeiss, Germany) and energy dispersive spectroscopy (EDS). Microhardness was measured using a Vickers hardness tester (HV-1000) with a 5 N load applied for 10 s. Surface roughness was measured by laser confocal microscope (OLS4000; Japan). Residual stresses of the samples were analyzed using an X-ray stress analyzer (HAOYUAN DST-17) with Cu Kα radiation, operating at 25 mA tube current, 25 kV tube voltage, a 2θ range of 150-170°, ψ angle range of 0-35°. The surfaces of the three types of processed samples were polished to different stress depths, preparing four samples of varying depths for each process sample. After polishing the surface, etch them with aqua regia for 10 s, measure the residual stress three times, and take the average value. Electro-polishing was performed on the cross-sections of the three samples of the cladding layer obtained through wire cutting, followed by observation using Electron Backscatter Diffraction (EBSD). The EBSD images were obtained using a Field Emission Scanning Electron Microscope (SEM, Zeiss Ultra 55) with a working voltage set at 20 kV and a tilt angle of 70°. Data was processed using HKL-Channel 5 software. The surface of LR-USR samples was observed using a Transmission Electron Microscope (TEM, FEI Tecnai F20).

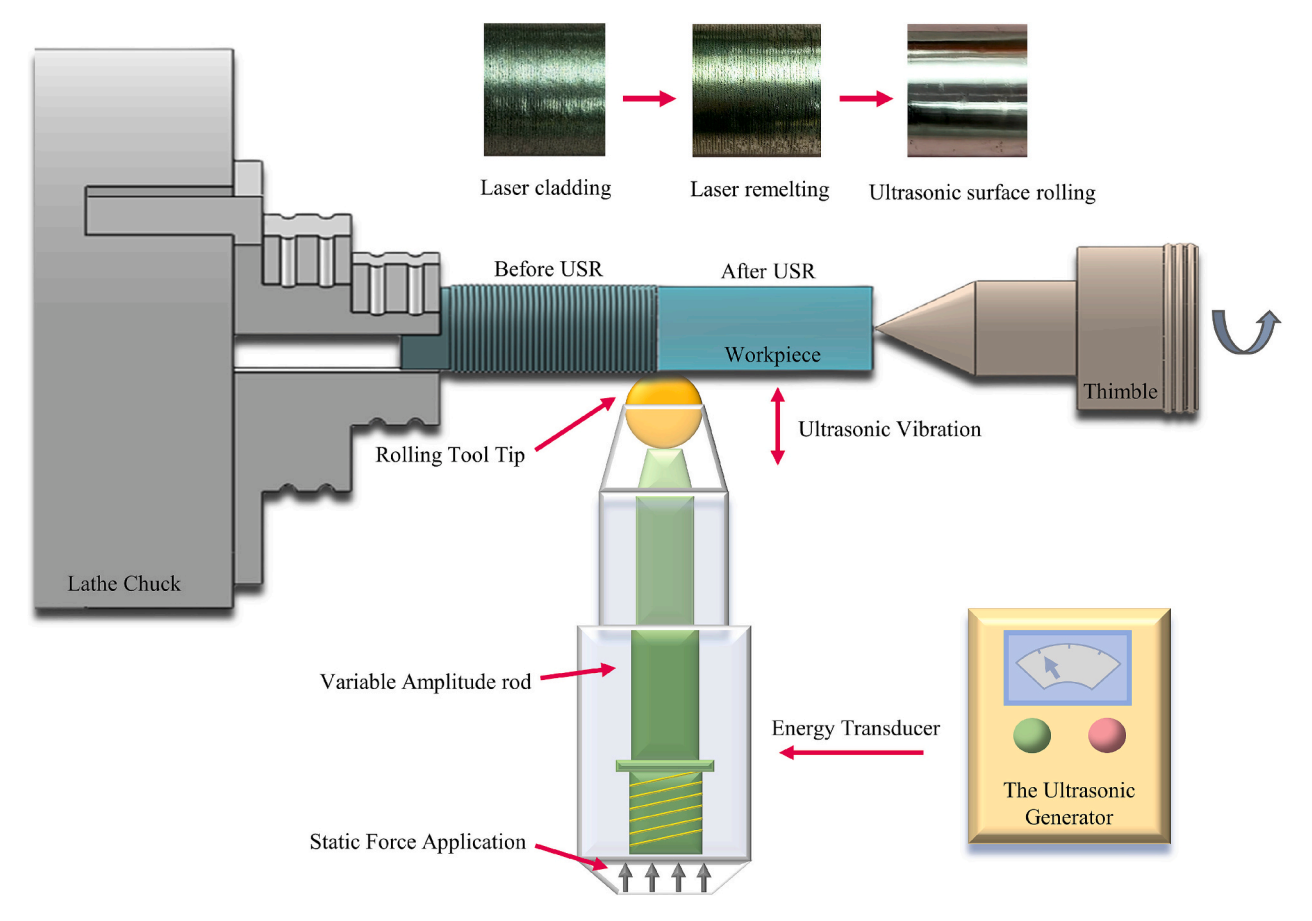


Fig. 2. Schematic diagram of ultrasonic surface rolling (USR).

## 2.3. Tribological test

Using a material surface properties tester (MFT-4000), the grinding ball is a  $\phi 5$  mm SiC ball with a hardness  $>\!2000$  HV. Linear reciprocating wear tests were conducted on the surfaces of each prepared sample under conditions of 20 N load, 5 mm reciprocating distance, 200 mm/min velocity, and 40 min loading time. The experiment was conducted

three times, and the average results were taken. Prior to testing, samples were ultrasonically cleaned in alcohol for 5 min. Three-dimensional wear surfaces of each sample were captured using a laser confocal microscope (OLS4000; Japan). The wear morphology was observed by field mission scanning electron microscopy (SEM; Zeiss, Germany).

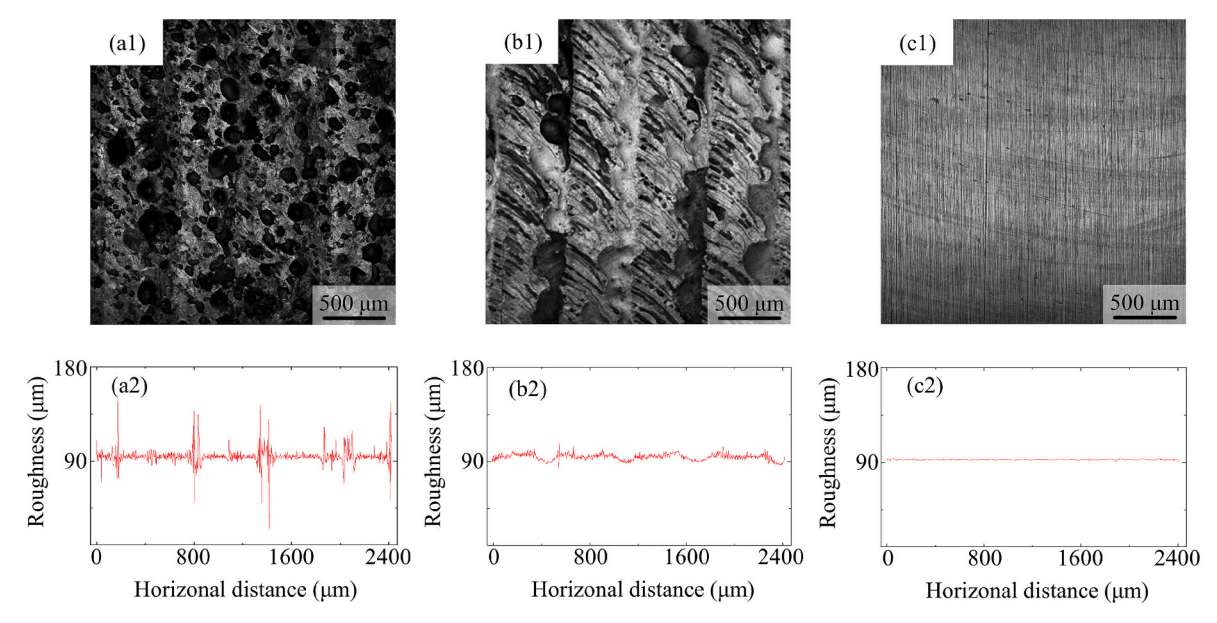


Fig. 3. Surface morphology and roughness of (a) LC, (b) LR, and (c) LR-USR samples.

#### 3. Results and discussions

#### 3.1. Surface roughness

Fig. 3 illustrates the surface morphology and roughness of LC, LR, and LR-USR. Pronounced laser track marks are evident on the surfaces of the LC and LR samples, resulting in uneven surfaces with grooves and ridges (Fig. 3(a1), (b1)). The roughness measurement of the LC sample surface is approximately 4.15  $\mu m$  (Fig. 3(a2)). Severe powder sticking is observed on the LC sample surface, primarily due to uneven laser energy distribution resulting in incomplete powder melting. After LR, the average roughness decreases to 2.35  $\mu m$  (Fig. 3(b2)), as a substantial amount of unmelted powder further melts and flows into the coating, smoothing the surface and reducing ridges and grooves. The LR-USR surface exhibits the highest smoothness (Fig. 3(c1)), with an average surface roughness reduced to 0.42  $\mu m$  (Fig. 3(c2)). Laser scanning tracks

disappear, and severe plastic deformation causes protrusions to fill into the grooves, resulting in a smooth surface. These results indicate that, without subtractive manufacturing, LC layer can achieve a surface with Ra  $<0.5~\mu m$  through subsequent processing. LR and USR can mitigate machining traces on LC and improve coating surface quality. However, achieving desired surface cleanliness requires parameter adjustments across all processes, necessitating further experimental validation for precise outcomes.

#### 3.2. Microstructure

To study the changes in grain size, and strain of the LC, LR, and LR-USR samples, EBSD data for the three samples were obtained near the surface of the cladding layer. It can be clearly seen from Fig. 4(a1)-(c1) that there has been a change in dendrite size. Compared to LC and LR, the dendrites in the LR-USR sample were significantly refined. The IPF

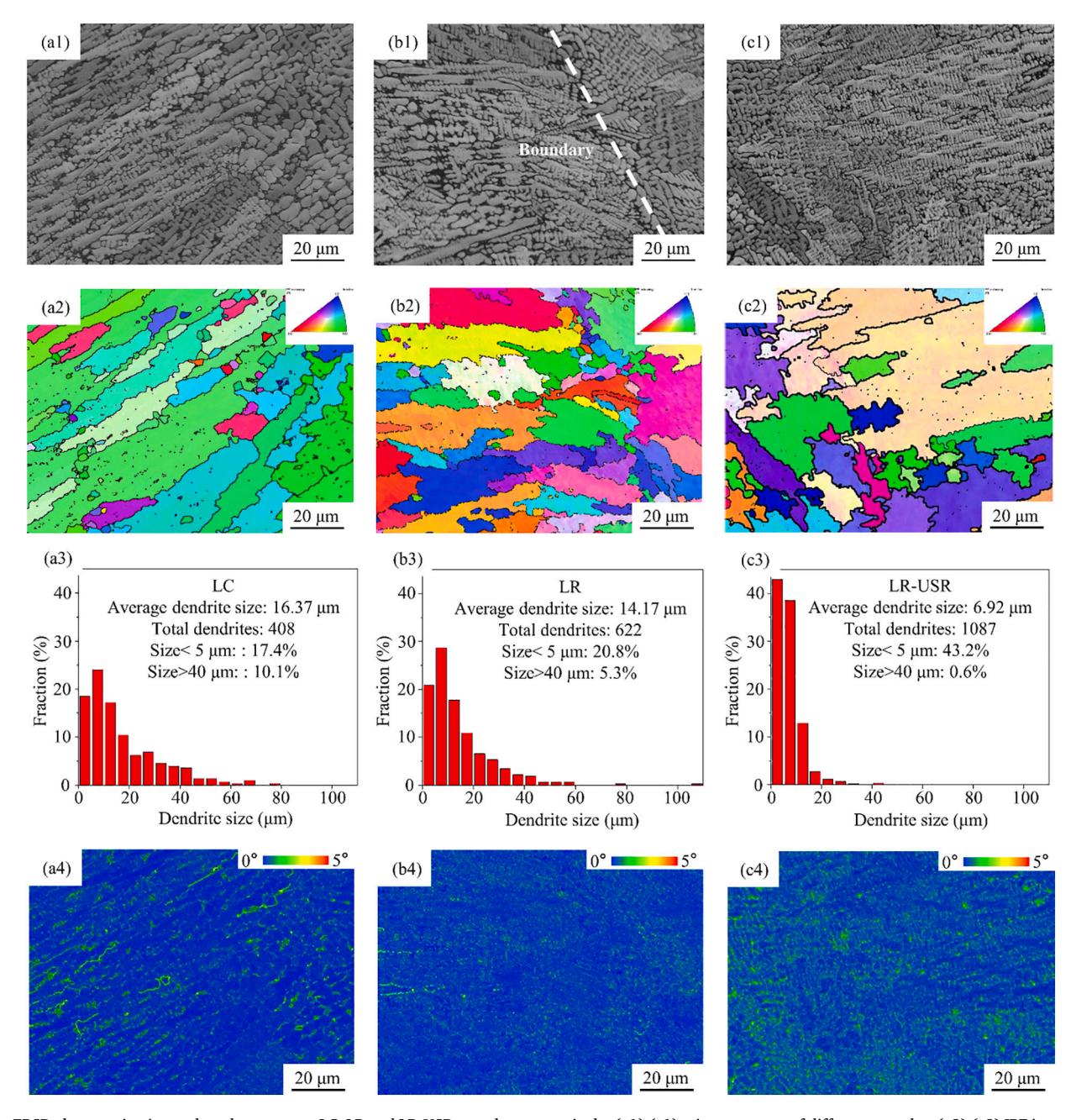


Fig. 4. EBSD characterization: a, b and c represent LC, LR and LR-USR samples, respectively. (a1)-(c1) microstructure of different samples, (a2)-(c2) IPF images, (a3)-(c3) dendrite size distributions, (a4)-(c4) KAM maps.

map of the LR sample shown in Fig. 4(b2) captured the interface between two adjacent layers of the cladding layer, where changes in grain size and grain orientation occur at the boundary. As shown in Fig. 4(a3)-(c3), the average dendrite size of the LR sample decreased from 16.37 μm to 14.17 μm. Due to the increased temperature gradient (G) in LR, the molten metal undergoes rapid solidification, reducing the solidification rate (R) and refining the dendritic structure [13]. The average dendrite size of the LR-USR sample decreased to 6.92 µm, and the proportion of LR-USR dendrites smaller than 5  $\mu m$  increased from 17.4 % in the LC to 43.2 %, while the proportion larger than 40  $\mu m$  decreased to 0.6 %. The KAM maps are shown in Fig. 4(a4)-(c4). KAM (Kernel Average Mismatch) during EBSD analysis can be used as a measure of local misorientation. Previous studies have reported the use of KAM to evaluate strain distribution and dislocation density distribution in microstructures [23,24]. Blue indicates a smaller local misorientations of grains, while green indicates a larger local misorientations [25,26]. From Fig. 4(c4), it can be observed that the local misorientations in the LR-USR coating is larger, primarily distributed in the interdendritic regions, indicating USR may cause dislocations within the grains, increasing the strain [20].

In order to study the impact of USR treatment on the surface microstructure, the cross-section of the LR-USR sample was observed using TEM (Fig. 5). In areas away from the top surface of the sample, a large number of stacking faults were found, as shown in Fig. 5(c). For Stellite 6 materials, stacking fault energy is relatively low, which makes stacking faults more likely to occur [27–29]. However, the large plastic deformation introduced by USR resulted in high-density dislocations within deformed grains, which are formed by the entanglement of a large number of dislocations [30,31], as shown in Fig. 5(a) and (b). Closer to the coating surface, the dislocation density increases with the increase in plastic deformation. Dense dislocations produce a high-density strain energy, under high-density strain, the internal grains undergo annihilation, accumulation, and rearrangement to form smaller grains. [18,32].

Fig. 6 illustrates the grain morphology of LR-USR cladding layer from the top surface through the interior to the interface with the substrate. At the top of the cladding layer (Fig. 6(a)), equiaxed grains are present, within the cladding layer (Fig. 6(b), (c)), typical columnar dendrites and equiaxed grains are observed. In the interfacial region between the cladding layer and substrate, non-dendritic microstructure areas are identified (Fig. 6(f)). Under conditions of rapid solidification and high cooling rates, the initial temperature gradient G within the cladding layer is small and the undercooling is low, resulting in a low number of nucleation. Nucleation occurs at partially melted particles, unmelted particles, and impurities [17]. As temperature decreases, undercooling increases, significantly accelerating nucleation rates, leading to preferential dendritic growth followed by equiaxed grain formation. Additionally, variations in dendrite size are observed. Significant changes in

dendrite size occur at the interface between two cladding layers, where the previous layer is in a semi-solid state upon the arrival of the later layer. Upon heating, numerous grains near the grain boundaries migrate swiftly, enveloping adjacent grain boundaries and facilitating their expansion, as depicted in Fig. 6(d), which shows larger grains. The initially larger grain size at the bottom of the cladding layer may be attributed to the higher thermal conductivity of 27SiMn steel (K = 27 W/(m·K)) compared to that of Stellite 6 (K = 14.82 W/(m·K)) [33]. When laser energy interacts with the powder flow on the substrate surface, causing melting of both, heat transfers from the interior of the substrate to adjacent layers near the substrate, resulting in increased grain size [34].

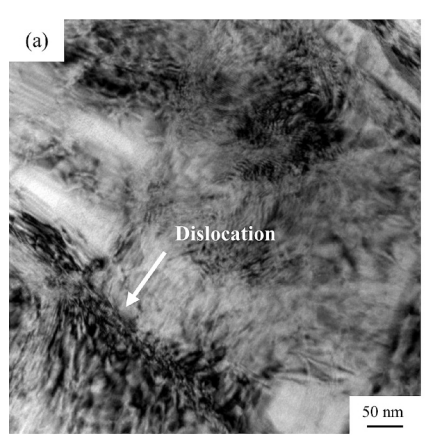
#### 3.3. Hardness and residual stress

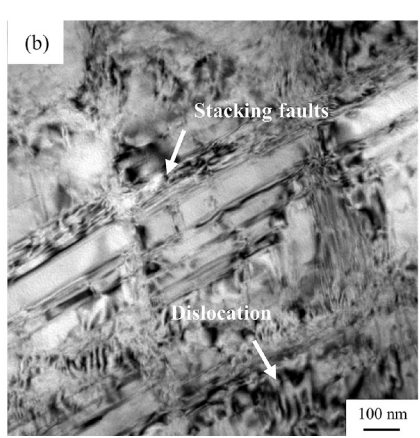
Fig. 7 shows the microhardness measured at different depths for LC, LR, and LR-USR samples. The LR ( $\sim$ 478 HV) shows an average microhardness increase of 5 % compared to the LC ( $\sim$ 455 HV) sample, which is due to laser-assisted grain refinement leading to an increase in hardness [35,36]. The average hardness of the LR-USR sample is 512 HV. At a distance of about 800  $\mu$ m from the LR-USR sample surface, the microhardness of USR ( $\sim$ 560 HV) is significantly higher than that of LR ( $\sim$ 492 HV) and LC ( $\sim$ 456 HV) samples, with an increase in hardness of 13.8 % and 22.8 %, respectively. This is due to the introduction of intense plastic deformation, which generates a large number of dislocations on the sample surface. To accommodate the large dislocation strain, the original grains are disrupted, forming numerous dislocation entanglements that create more grain boundaries and densification of grains, leading to an increase in hardness [20,31].

Fig. 8 shows the variation of residual stress with depth in the samples. LC induced TRS on the outer surface, with a maximum value of approximately 225 MPa. After LR, the TRS on the outer surface increased to about 290 MPa. This may be due to the fact that, although the laser power of LR is the same as that of LC, the laser absorption rate of powder to solid is different, resulting in a higher cooling rate and thermal gradient, which increases the TRS on the outer surface [37]. USR transformed the TRS into CRS, with a CRS depth >150  $\mu m$ . The maximum measured surface value was about -370 MPa because USR introduced large strain to the surface, and the continuously increasing strain rate caused high-density dislocations to move, forming dislocation entanglements. At this point, the grains were refined, and stress was stored within the grains, thus generating a larger CRS [18].

### 3.4. Friction and wear behavior

The average friction coefficient for LC, LR, LR-USR samples is shown in Fig. 9(a). The friction coefficient of the LR-USR sample is lower than that of LC and LR samples, with the friction coefficient decreasing from





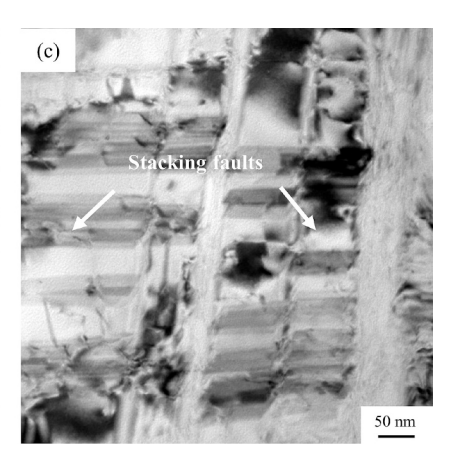


Fig. 5. TEM image of LR-USR sample: (a) at a depth of 30 μm, (b) at a depth of 50 μm, (c) at a depth of 100 μm.

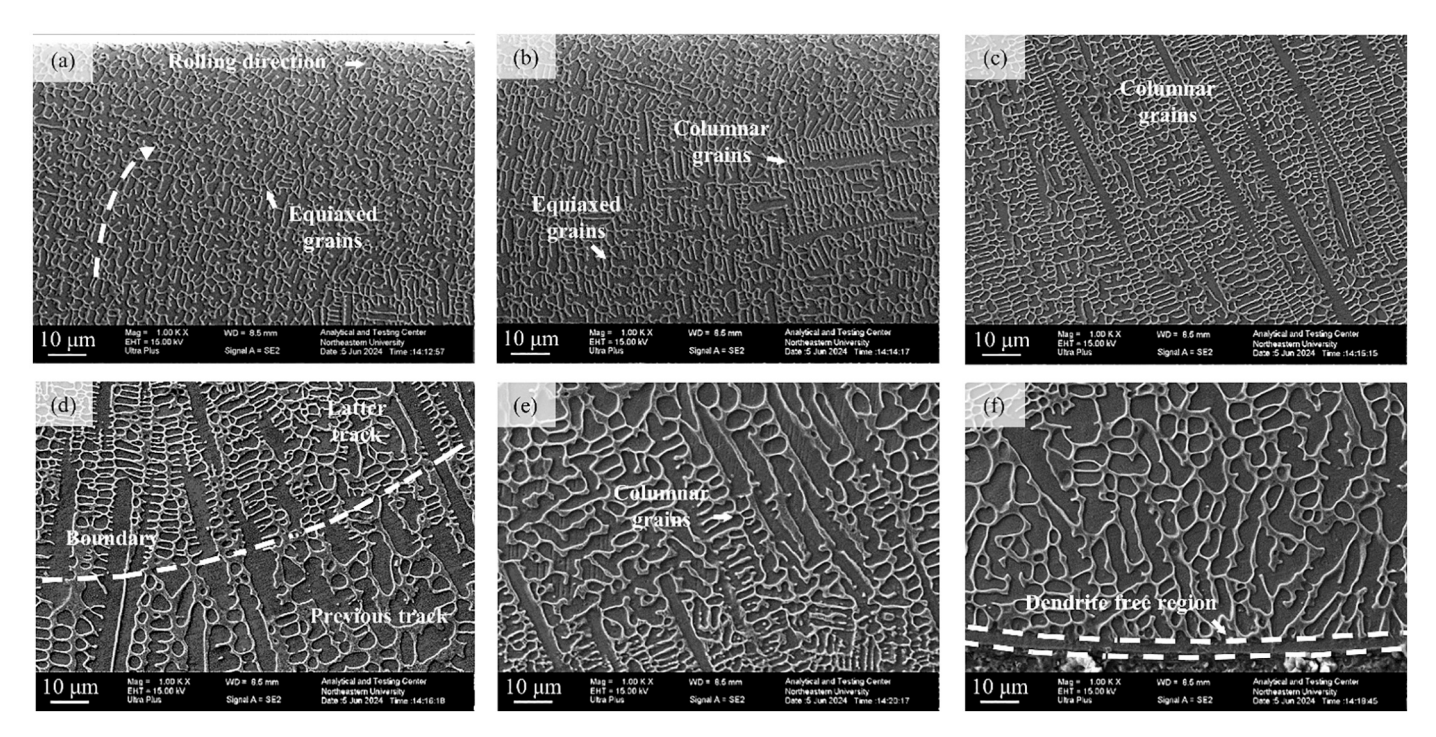


Fig. 6. The grain morphology of LR-USR from (a) the top of the cladding layer, (b-e) the interior of the cladding layer, (f) the junction between the cladding layer and the substrate.

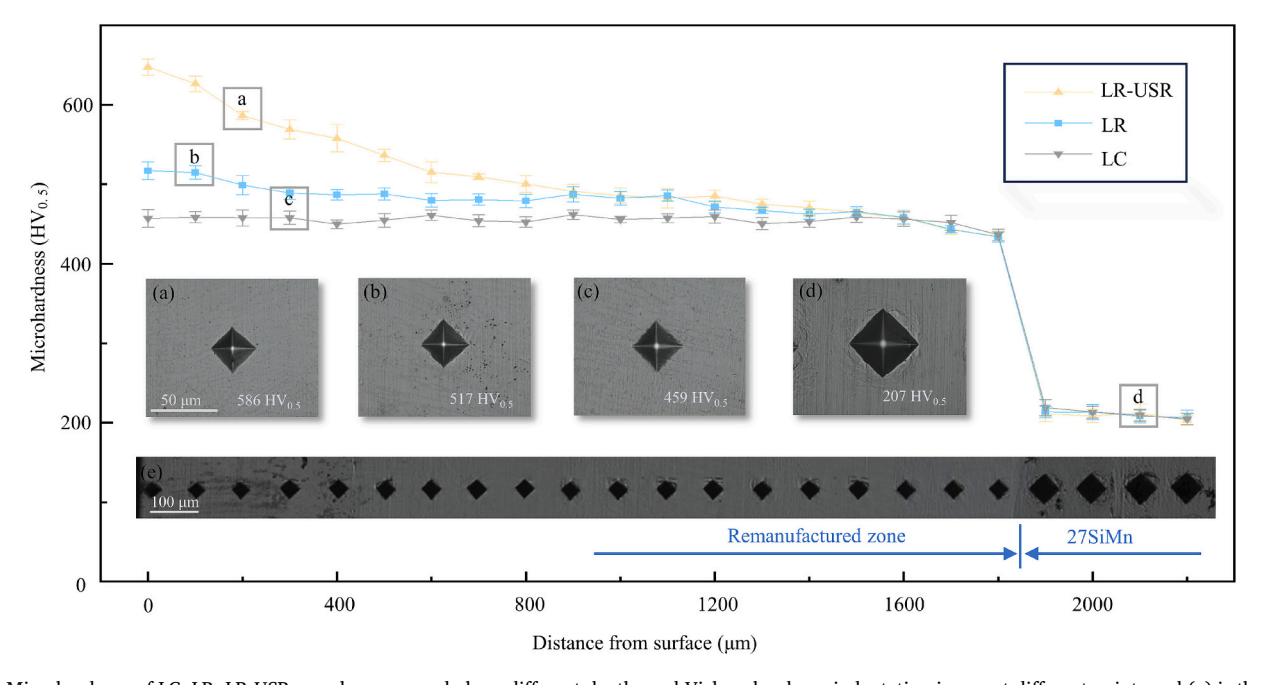


Fig. 7. Microhardness of LC, LR, LR-USR samples measured along different depths and Vickers hardness indentation image at different points and (e) is the overall indentation morphology of LR-USR sample in depth direction.

0.423 to 0.405 after LR, and further decreasing to 0.380 after USR. This is because the deformed surface from USR introduces higher CRS and higher hardness, which hinders the delamination damage of the wear surface by the friction ball [38].

Fig. 9(b) shows section curves of samples after the wear test. And the Fig. 9(c)-(e) show the local 3D profile. The wear tracks on the LC sample are deeper and wider. After subsequent LR and USR, the wear tracks gradually become narrower and shallower, with the depth decreasing from  $10.1~\mu m$  to  $7.7~\mu m$  and  $6.1~\mu m$ , respectively. Since the friction wear test is conducted on a cylindrical surface, the volume of wear loss cannot

be obtained by measurement, but the volume of wear depth can be obtained (as shown in Fig. 9(a)). From the volume of wear depth, it can be known that the LR-USR sample has the best wear resistance, with the wear depth volume being approximately half that of the LC sample. The results indicate that both LR and USR can improve the wear resistance of the samples, with LR-USR further enhancing it.

To clarify the mechanisms by which the three different treatment methods affect friction wear performance, SEM analysis was conducted on the micro-morphology of the wear marks. As seen in Fig. 10(a)-(c), the surface of Stellite 6 material after SiC wear is overall smooth and

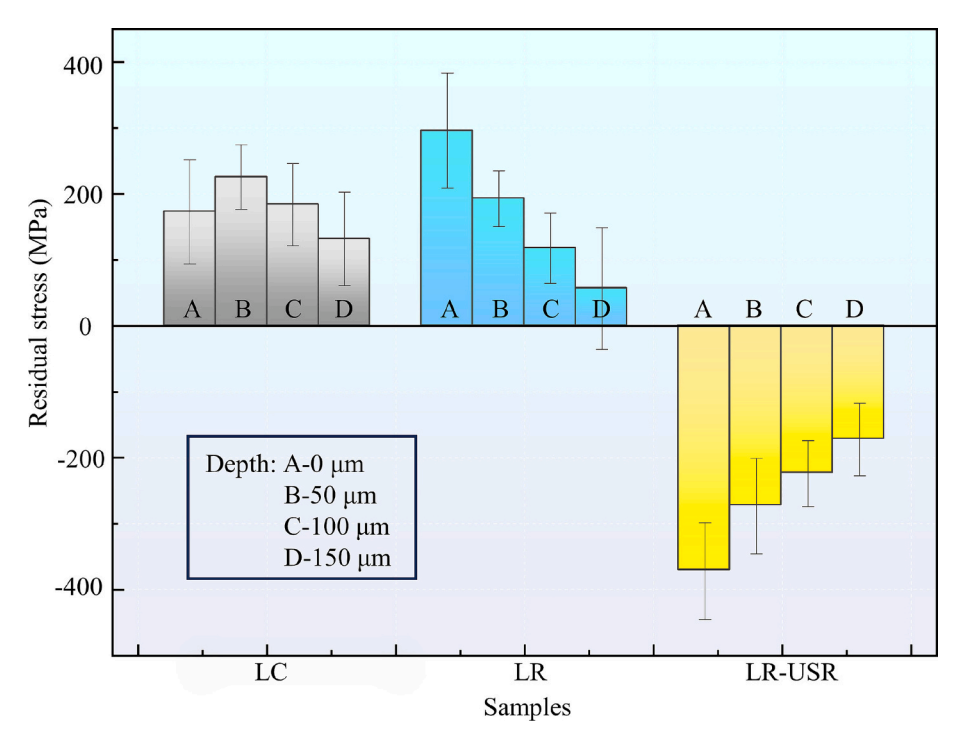


Fig. 8. Residual stress of different samples.

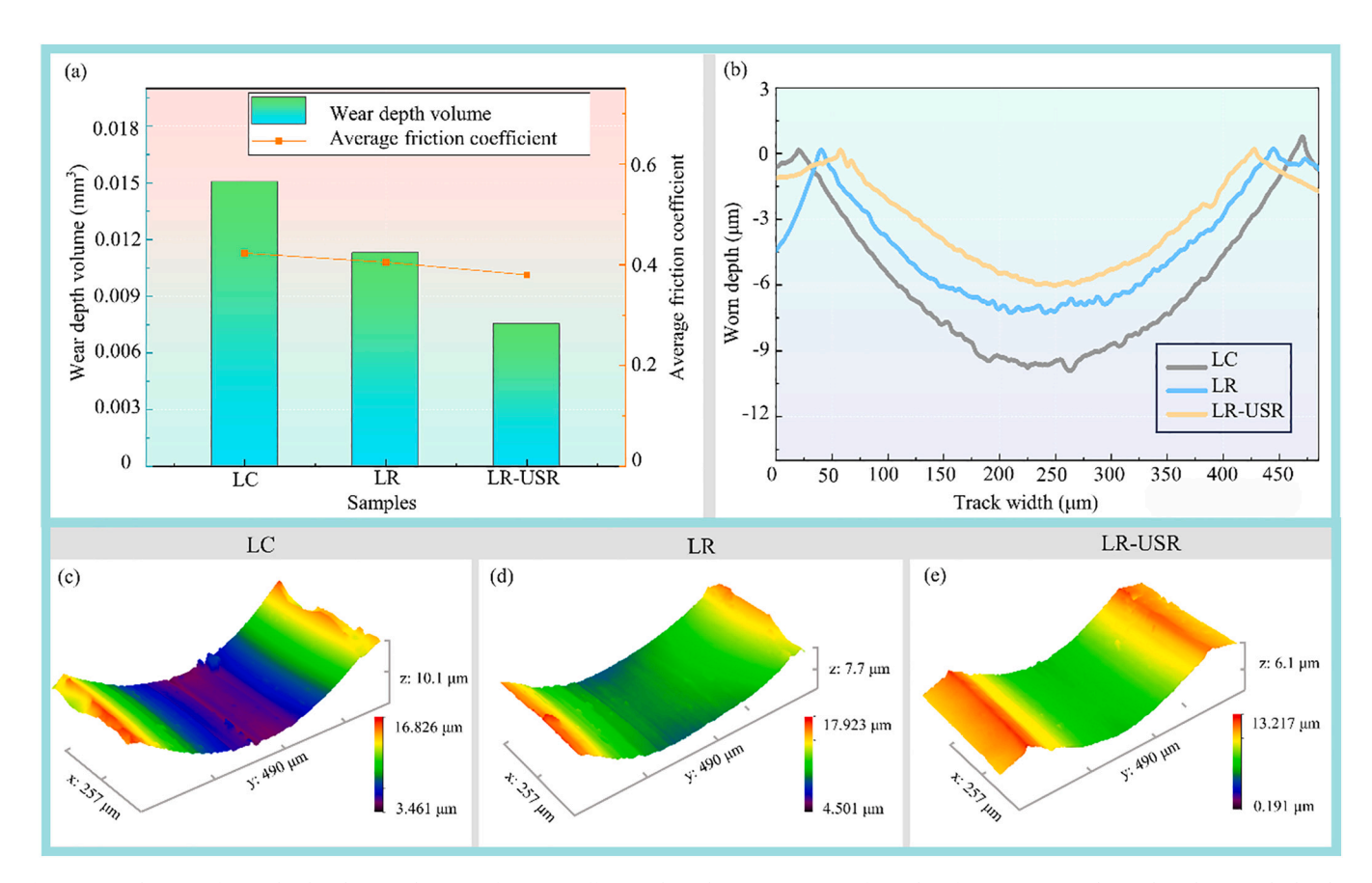


Fig. 9. (a) is the map of wear depth volume and average friction coefficient, (b) is the section curves of samples after wear test, and (c), (d) and (e) are the local 3D profile of the samples after wear test, respectively.

even, without large-scale delamination, primarily exhibiting abrasive wear, consistent with the findings in [39,40]. However, as seen in Fig. 10 (a), the LC worn sample exhibits a greater number of grooves and

instances of delamination. This phenomenon occurs as material from the surface of the cladding layer peels off, forming abrasive chips during sliding. These chips roll on the surface of the cladding layer and further

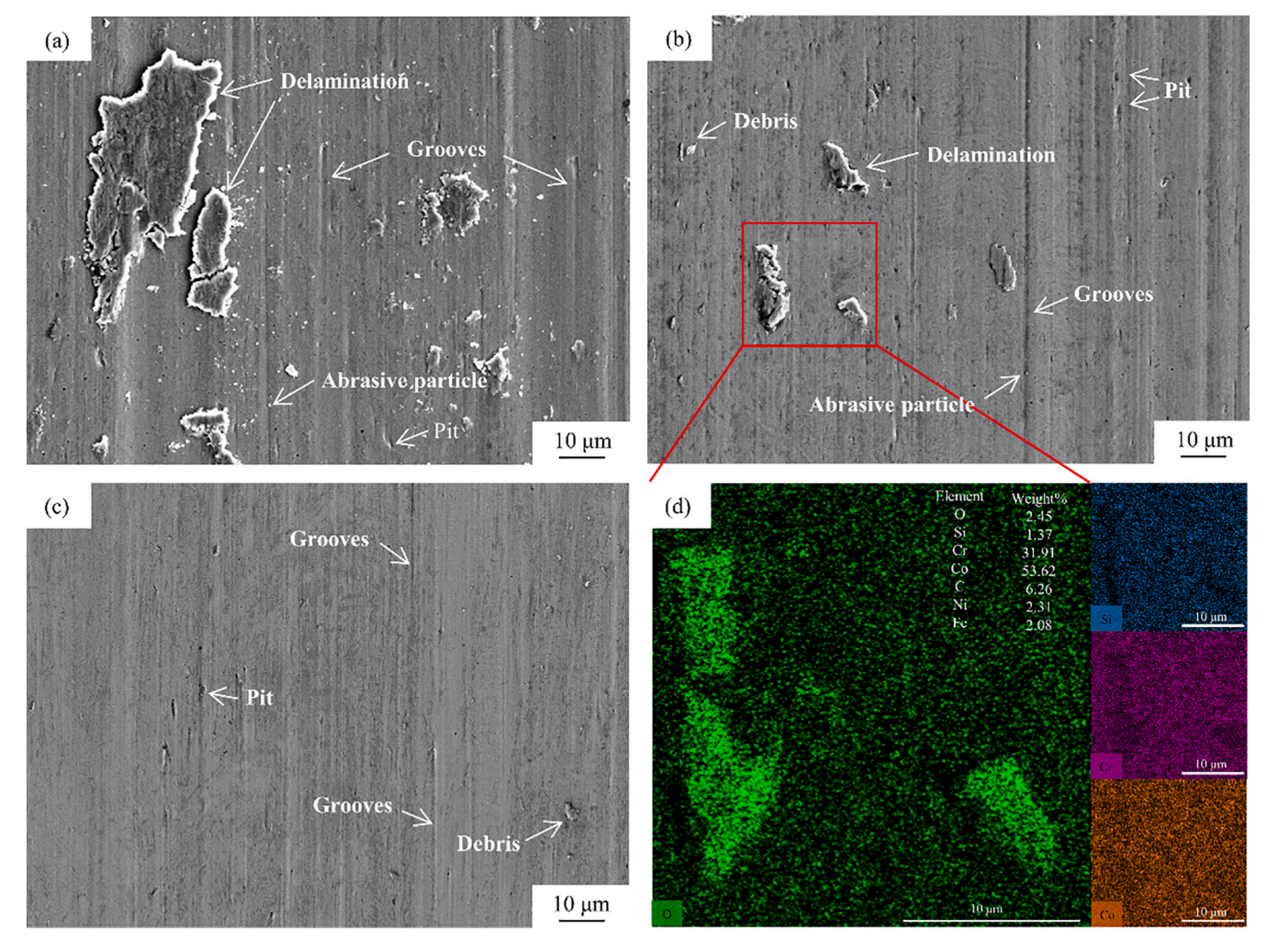


Fig. 10. (a), (b) and (c) are the wear morphologies of samples LC, LR and LR-USR, respectively, and (d) is the EDS map at delamination.

act as abrasives, forming abrasive particles, which result in more grooves and chips [41]. From Fig. 10(b), it can be seen that the LR sample also has some grooves and abrasive particles remaining on the worn surface, but the wear rate is reduced compared to the LC sample. This is because the densification caused by laser remelting leads to increased hardness, resulting in a decrease in the volume of the wear ball embedded in the coating [42]. The wear mechanism is primarily abrasive wear, with a minor amount of spalling. Fig. 10(d) shows the distribution maps of the main elements from EDS at the delamination area. Based on the distribution of elements, it can be inferred that the flaky delamination on the wear surface is composed of oxides. Fig. 10(c) shows the micro-morphology of the worn surface of the LR-USR sample. Compared to the LC and LR samples, the LR-USR sample has a significantly reduced number of grooves on the worn surface, narrower groove widths, and a decrease in the depth of the micro convex embedded in the coating surface. This is due to the refinement of grains and higher hardness within the LR-USR sample, which enhances the wear resistance of the coating. Additionally, USR has induced higher CRS on the coating surface, inhibiting the formation of delamination [43]. The wear mechanism of the LR-USR sample is characterized by typical abrasive wear.

## 4. Conclusions

Explored in this study is the effects of LR followed by USR on the microstructure, mechanical properties, and frictional wear behavior of LC Stellite 6 alloy coatings. The following conclusions can be drawn:

- 1. LR-USR reduced the surface roughness of the LC sample to  $0.42~\mu m$ . LR-USR significantly refined the dendrites in the coating layer, with the average size of the dendrites decreasing to  $6.92~\mu m$ .
- The internal strain within the grains of the LR-USR samples increased significantly, and a high-density of dislocations was generated within the grains near the coating surface.
- 3. At approximately 800  $\mu$ m from the LR-USR surface, the microhardness of the USR (~560 HV) was significantly higher than that of LR (~492 HV) and LC (~456 HV), representing increases of 13.8 % and 22.8 %, respectively. USR transformed TRS into CRS.
- 4. The LR-USR samples exhibited the lowest friction coefficient, with a wear depth volume about half that of the LC samples. The wear mechanism of the LR-USR samples was characteristic of typical abrasive wear.

### CRediT authorship contribution statement

Jiayu Sun: Writing – review & editing, Writing – original draft, Conceptualization. Yingying Zhang: Methodology. Zhengyu Sun: Validation. Tianbiao Yu: Supervision, Resources, Project administration, Funding acquisition, Conceptualization. Guofa Wang: Supervision.

#### **Declaration of competing interest**

The authors declare that they have no known competing financial interests or personal relationships that could have appeared to influence the work reported in this paper.

#### Acknowledgments

The authors gratefully acknowledge the financial support of the National Natural Science Foundation of China [Grant number 52075088] and Liaoning Provincial Key Laboratory of Large Equipment Intelligent Design and Manufacturing Technology [Grant number 18006001].

#### Data availability

Data will be made available on request.

#### References

- P. Zhang, Z. Liu, On sustainable manufacturing of Cr-Ni alloy coatings by laser cladding and high-efficiency turning process chain and consequent corrosion resistance, J. Clean. Prod. 161 (2017) 676–687, https://doi.org/10.1016/j. iclepro.2017.05.169.
- [2] N. Khanna, P. Raval, D. Patel, R. Prajapati, J. Schoop, K.K. Gajrani, Assessment of additive and subtractive sustainable manufacturing of Inconel 625, Tribol. Int. 186 (2023) 108655, https://doi.org/10.1016/j.triboint.2023.108655.
- [3] B. Xu, Green remanufacturing engineering and its development strategy in China, Front. Eng. Manag. 3 (185) (2016) 102–106, https://doi.org/10.15302/j-fem-2016024.
- [4] M. Attaran, The rise of 3-D printing: the advantages of additive manufacturing over traditional manufacturing, Bus. Horiz. 60 (2017) 677–688, https://doi.org/ 10.1016/j.bushor.2017.05.011.
- [5] L. Zhou, G. Ma, H. Zhao, H. Mou, J. Xu, W. Wang, Z. Xing, Y. Li, W. Guo, H. Wang, Research status and prospect of extreme high-speed laser cladding technology, Opt. Laser Technol. 168 (2024) 109800, https://doi.org/10.1016/j. optlaster 2023 109800
- [6] L. Zhu, P. Xue, Q. Lan, G. Meng, Y. Ren, Z. Yang, P. Xu, Z. Liu, Recent research and development status of laser cladding: a review, Opt. Laser Technol. 138 (2021) 106915, https://doi.org/10.1016/j.optlastec.2021.106915.
- [7] Y. Bao, J. Deng, S. Cao, K. Ma, Z. Zhang, Y. Lu, Laser micro-cladding in situ forming textured surface to improve the tribological performance, Wear 550 (2024) 205422, https://doi.org/10.1016/j.wear.2024.205422.
- [8] X. Liu, L. Meng, X. Zeng, B. Zhu, K. Wei, J. Cao, Q. Hu, Studies on high power laser cladding Stellite 6 alloy coatings: metallurgical quality and mechanical performances, Surf. Coat. Technol. 481 (2024) 130647, https://doi.org/10.1016/j. surfcoat.2024.130647.
- [9] J. Sun, H. Lu, N. Tu, H. Yang, W. Wang, F. Guo, Friction and corrosion characteristics of microarc oxidation/laser cladding palygorskite coating on 6061 aluminum alloy substrates, Surf. Coat. Technol. 487 (2024) 130992, https://doi. org/10.1016/j.surfcoat.2024.130992.
- [10] K. Qi, Y. Yang, W. Liang, K. Jin, L. Xiong, Influence of the anomalous elastic modulus on the crack sensitivity and wear properties of laser cladding under the effects of a magnetic field and Cr addition, Surf. Coat. Technol. 423 (2021) 127575, https://doi.org/10.1016/j.surfcoat.2021.127575.
- [11] P. Zhang, Z. Liu, Effect of sequential turning and burnishing on the surface integrity of Cr-Ni based stainless steel formed by laser cladding process, Surf. Coat. Technol. 276 (2015) 327–335, https://doi.org/10.1016/j.surfcoat.2015.07.026.
- [12] S. Huang, S. Qiao, C. Shao, L. Li, S. Li, D. Deng, F. Lu, Study on residual stress evolution of laser cladding low chromium carbon alloy on low-pressure rotor, J. Manuf. Process. 85 (2023) 31–42, https://doi.org/10.1016/j. images 2022.11.042
- [13] A.K. Praharaj, J.K. Chaurasia, G.R. Chandan, S. Bontha, P.S. Suvin, Enhanced tribological performance of laser directed energy deposited Inconel 625 achieved through laser surface remelting, Surf. Coat. Technol. 477 (2024) 130345, https:// doi.org/10.1016/j.surfcoat.2023.130345.
- [14] Y. Zhao, J. Sun, J. Li, Study on chip morphology and milling characteristics of laser cladding layer, Int. J. Adv. Manuf. Technol. 77 (2015) 783–796, https://doi.org/ 10.1007/s00170-014-6483-2.
- [15] Y. Zhao, J. Sun, J. Li, Effect of rare earth oxide on the properties of laser cladding layer and machining vibration suppressing in side milling, Appl. Surf. Sci. 321 (2014) 387–395, https://doi.org/10.1016/j.apsusc.2014.09.195.
- [16] P. Zhang, Z. Liu, Enhancing surface integrity and corrosion resistance of laser cladded Cr–Ni alloys by hard turning and low plasticity burnishing, Appl. Surf. Sci. 409 (2017) 169–178, https://doi.org/10.1016/j.apsusc.2017.03.028.
- [17] H. Ye, J. Zhu, Y. Liu, W. Liu, D. Wang, Microstructure and mechanical properties of laser cladded Cr–Ni alloy by hard turning (HT) and ultrasonic surface rolling (USR), Surf. Coat. Technol. 393 (2020) 125806, https://doi.org/10.1016/j. surfcoat.2020.125806.
- [18] Z. Wang, Z. Liu, C. Gao, K. Wong, S. Ye, Z. Xiao, Modified wear behavior of selective laser melted Ti6Al4V alloy by direct current assisted ultrasonic surface rolling process, Surf. Coat. Technol. 381 (2020) 125122, https://doi.org/10.1016/ j.surfcoat.2019.125122.

- [19] J. Hao, Q. Niu, H. Ji, H. Liu, Effect of ultrasonic rolling on the organization and properties of a high-speed laser cladding IN 718 Superalloy coating, Crystals 13 (2023) 1214, https://doi.org/10.3390/cryst13081214.
- [20] X. Luo, X. Ren, Q. Jin, H. Qu, H. Hou, Microstructural evolution and surface integrity of ultrasonic surface rolling in Ti6Al4V alloy, J. Mater. Res. Technol-JMR&T 13 (2021) 1586–1598, https://doi.org/10.1016/j.jmrt.2021.05.065.
- [21] S. Qu, J. Wang, X. Hu, F. Lai, Y. Deng, X. Li, Effect of ultrasonic nanocrystalline surface modification process on fretting wear behavior of laser surface textured 20CrMoH steel, Surf. Coat. Technol. 427 (2021) 127827, https://doi.org/10.1016/ i.surfcoat.2021.127827.
- [22] W. Ting, W. Dongpo, L. Gang, G. Baoming, S. Ningxia, Investigations on the nanocrystallization of 40Cr using ultrasonic surface rolling processing, Appl. Surf. Sci. 255 (2008) 1824–1829, https://doi.org/10.1016/j.apsusc.2008.06.034.
- [23] C. Tao, J. Fan, L. Wu, H. Yi, Grain refinement and strain delocalization in TRIP high-entropy alloys during hot deformation, Mater. Today Commun. 39 (2024) 109272, https://doi.org/10.1016/j.mtcomm.2024.109272.
- [24] Y. Peng, L. Wang, C. Liu, C. Xu, L. Geng, G. Fan, Revealing the exceptional cryogenic strength-ductility synergy of a solid solution 6063 alloy by in-situ EBSD experiments, J. Mater. Sci. Technol. 208 (2025) 313–322, https://doi.org/ 10.1016/j.jmst.2024.03.081.
- [25] M.N. Gussev, D.A. McClintock, T.S. Byun, T.G. Lach, Recent progress in analysis of strain-induced phenomena in irradiated metallic materials and advanced alloys using SEM-EBSD in-situ tensile testing, Curr. Opin. Solid State Mater. Sci. 28 (2024) 101132, https://doi.org/10.1016/j.cossms.2023.101132.
- [26] L. Liu, W. Huang, M. Ruan, Z. Chen, Effects of temperatures on microstructure evolution and deformation behavior of Fe–32Ni by in-situ EBSD, Mater. Sci. Eng. A-Struct. Mater. Prop. Microstruct. Process. 875 (2023) 145097, https://doi.org/ 10.1016/j.msea.2023.145097.
- [27] M.M. Bakhshayesh, F. Khodabakhshi, M.H. Farshidianfar, S. Nagy, M. Mohammadi, G. Wilde, Additive manufacturing of Stellite 6 alloy by laser-directed energy deposition: engineering the crystallographic texture, Mater Charact 207 (2024) 113511, https://doi.org/10.1016/j.matchar.2023.113511.
- [28] B. Chen, R. Chen, Y. Fan, Z. Chen, Z. Zhao, Microstructural characterization of Stellite 6 alloy processed by electron beam melting, Vacuum 229 (2024) 113591, https://doi.org/10.1016/j.vacuum.2024.113591.
- [29] J. Xiong, H. Zhang, F. Nie, F. He, J. Yang, Z. Hu, Z. Wen, H. Zhao, X. Yuan, Formation mechanisms for (Cr,Co)<sub>7</sub>C<sub>3</sub>/(Cr,Co)<sub>23</sub>C<sub>6</sub> heterogeneous precipitates and stacking faults around carbides in surfacing welding of stellite alloy on stainless steel, Met. Mater. Int. 28 (2022) 1639–1649, https://doi.org/10.1007/s12540-021-01049-9.
- [30] P. Wang, H. Guo, D. Wang, H. Duan, Y. Zhang, Microstructure and tribological performances of M50 bearing steel processed by ultrasonic surface rolling, Tribol. Int. 175 (2022) 107818, https://doi.org/10.1016/j.triboint.2022.107818.
- [31] F. Lai, S. Qu, R. Lewis, T. Slatter, W. Fu, X. Li, The influence of ultrasonic surface rolling on the fatigue and wear properties of 23-8N engine valve steel, Int. J. Fatigue 125 (2019) 299–313, https://doi.org/10.1016/j.ijfatigue.2019.04.010.
- [32] G. Li, S. Qu, M. Xie, Z. Ren, X. Li, Effect of multi-pass ultrasonic surface rolling on the mechanical and fatigue properties of HIP Ti-6Al-4V alloy, Materials 10 (2017) 133, https://doi.org/10.3390/ma10020133.
- [33] M. Moradi, A. Ashoori, A. Hasani, Additive manufacturing of stellite 6 superalloy by direct laser metal deposition – part 1: effects of laser power and focal plane position, Opt. Laser Technol. 131 (2020) 106328, https://doi.org/10.1016/j. optlastec 2020 106328
- [34] X. Zhan, C. Qi, Z. Gao, D. Tian, Z. Wang, The influence of heat input on microstructure and porosity during laser cladding of invar alloy, Opt. Laser Technol. 113 (2019) 453-461. https://doi.org/10.1016/j.optlastec.2019.01.015
- Technol. 113 (2019) 453–461, https://doi.org/10.1016/j.optlastec.2019.01.015.
  [35] D.P. Karmakar, G. Muvvala, A.K. Nath, High-temperature abrasive wear characteristics of H13 steel modified by laser remelting and cladded with Stellite 6 and Stellite 6/30% WC, Surf. Coat. Technol. 422 (2021) 127498, https://doi.org/10.1016/j.surfonat.2021.127498.
- [36] F. Ge, H. Yuan, Q. Gao, T. Peng, S. Guo, P. Lyu, Q. Guan, H. Liu, X. Liu, J. Guan, Microstructure, hardness and wear resistance of AlCoCrFeNiTax (x = 0, 0.1, 0.3) high-entropy alloys enhanced by laser remelting and Ta addition, J. Alloys Compd. 949 (2023) 169741, https://doi.org/10.1016/j.jallcom.2023.169741.
- [37] B. Das, A.K. Nath, P.P. Bandyopadhyay, Online monitoring of laser remelting of plasma sprayed coatings to study the effect of cooling rate on residual stress and mechanical properties, Ceram. Int. 44 (2018) 7524–7534, https://doi.org/ 10.1016/j.ceramint.2018.01.152.
- [38] Y.C. Zhao, Y. He, J. Zhang, C. Meng, X. Zhang, S. Zhang, Effect of high temperature-assisted ultrasonic surface rolling on the friction and wear properties of a plasma sprayed Ni/WC coating on #45 steel substrate, Surf. Coat. Technol. 452 (2023) 129049, https://doi.org/10.1016/j.surfcoat.2022.129049.
- [39] Z. Chen, H. Yan, P. Zhang, Z. Yu, Q. Lu, J. Guo, Microstructural evolution and wear behaviors of laser-clad Stellite 6/NbC/h-BN self-lubricating coatings, Surf. Coat. Technol. 372 (2019) 218–228, https://doi.org/10.1016/j.surfcoat.2019.04.083.
- [40] A.C. Bozzi, F.D. Ramos, D.B.O. Vargas, Microabrasive wear behavior of different stellites obtained by laser cladding and casting processes, Wear 524 (2023) 204857, https://doi.org/10.1016/j.wear.2023.204857.
- [41] L. Chen, Y. Zhao, F. Meng, T. Yu, Z. Ma, S. Qu, Z. Sun, Effect of TiC content on the microstructure and wear performance of in situ synthesized Ni-based composite

- coatings by laser direct energy deposition, Surf. Coat. Technol. 444 (2022) 128678, https://doi.org/10.1016/j.surf.coat.2022.128678
- https://doi.org/10.1016/j.surfcoat.2022.128678.

  [42] R. Deng, H. Li, C. Zhao, C. Ouyang, R. Wei, R. Wang, Q. Bai, Y. Liu, Study on the effect of laser Remelting energy density on the microstructure and Wear resistance of Fe-based alloy coatings fabricated by laser cladding, J. Alloys Compd. 33 (2024) 1455–1471, https://doi.org/10.1007/s11666-024-01795-3.
- [43] C. Chen, A. Feng, Y. Wei, Y. Wang, X. Pan, X. Song, Effects of WC particles on microstructure and wear behavior of laser cladding Ni60 composite coatings, Opt. Laser Technol. 163 (2023) 109425, https://doi.org/10.1016/j. optlastec.2023.109425.